PhotoniX

RESEARCH

Open Access

Optical steelyard: high-resolution and wide-range refractive index sensing by synergizing Fabry–Perot interferometer with metafibers

Lei Zhang[1,2,3], Xinggang Shang[2,3], Simin Cao[4], Qiannan Jia[1,2,3], Jiyong Wang[5*], Wei Yan[2,3*] and Min Qiu[2,3,4*]

*Correspondence:
jiyongwang@hdu.edu.cn;
yanwei@westlake.edu.cn;
qiumin@westlake.edu.cn

[1] College of Information Science and Electronic Engineering, Zhejiang University, Hangzhou 310027, China
[2] Key Laboratory of 3D Micro/Nano Fabrication and Characterization of Zhejiang Province, School of Engineering, Westlake University, 18 Shilongshan RoadZhejiang Province, Hangzhou 310024, China
[3] Institute of Advanced Technology, Westlake Institute for Advanced Study, 18 Shilongshan RoadZhejiang Province, Hangzhou 310024, China
[4] Westlake Institute for Optoelectronics, Fuyang, Hangzhou 311421, China
[5] Ministry of Education Engineering Research Center of Smart Microsensors and Microsystems, School of Electronics and Information, Hangzhou Dianzi University, Hangzhou 310018, China

Abstract
Refractive index (RI) sensors play an important role in various applications including biomedical analysis and food processing industries. However, developing RI sensors with both high resolution and wide linear range remains a great challenge due to the tradeoff between quality (*Q*) factor and free spectral range (*FSR*) of resonance mode. Herein, the optical steelyard principle is presented to address this challenge by synergizing resonances from the Fabry–Perot (FP) cavity and metasurface, integrated in a hybrid configuration form on the end facet of optical fibers. Specifically, the FP resonance acting like the scale beam, offers high resolution while the plasmonic resonance acting like the weight, provides a wide linear range. Featuring asymmetric Fano spectrum due to modal coupling between these two resonances, a high *Q* value (~ 3829 in liquid) and a sensing resolution (figure of merit) of 2664 RIU^{-1} are experimentally demonstrated. Meanwhile, a wide RI sensing range (1.330–1.430 in the simulation and 1.3403–1.3757 in the experiment) is realized, corresponding to a spectral shift across several *FSR*s (four and two *FSR*s in the simulation and experiment, respectively). The proposed steelyard RI sensing strategy is promising in versatile monitoring applications, e.g., water salinity/turbidity and biomedical reaction process, and could be extended to other types of sensors calling for both high resolution and wide linear range.

Keywords: Refractive index sensor, Fabry–Perot interferometer, Metafiber, High quality factor, Wide free spectral range, Fano resonance

Introduction

Profiting from light weight and real-time detection while serving as an integrated waveguide to introduce and interrogate light, optical fiber sensors have gained significant attention [1–3]. Depending on the region where light-matter interactions occur, optical fiber sensors could be categorized into sidewall integration and fiber tip integration [4, 5]. Nowadays, facing with the trend of the device miniaturization, fiber tip integrated sensors (FTISs) offer competitive advantages in compact size and instantaneous readout of complex fields (e.g., mechanical force, electromagnetic spectrum, acoustic oscillation) [4]. These benefits have motivated the research of FTISs in several directions, including ultrahigh-resolution force sensing [6, 7], temperature [8] and humidity [9] monitoring, electric [10] and magnetic [11] field detection, biosensor for point-of-care testing [12, 13], and concentration calibration of gas/liquid mixtures [14, 15], to name a few. In most of these applications, the external stimuli give rise to the change of refractive index (RI), making RI analysis one of the fundamental methods to detect the change of the measured quantities.

The performance of a sensor is evaluated by three pivotal parameters, i.e., sensitivity, resolution, and linear operating range [16–18]. For an FTIS, the RI change of the measurand is generally inferred from spectral shift of a resonance mode. Therefore, the sensitivity is routinely defined as the ratio of the change in resonance wavelength to the RI variations, that is S equals to $\Delta\lambda_{res}/\Delta n$, which reflects the degree of light-matter interactions. The resolution, also termed as figure of merit (*FoM*), is the normalized sensitivity to the full width at half maximum (*FWHM*) of the resonance, that is *FoM* equals to $S/FWHM$. The resolution determines the precision of an RI sensor. FoM is proportional to the quality (Q) factor, given that *FWHM* equals to λ_{res}/Q. Accordingly, *FoM* can be expressed as $S^{*}Q/\lambda_{res}$. The linear operating range, related to the free spectral range (*FSR*), governs the effective working range, within which the RI-response recalibration is unnecessary even in presence of large RI variations. Thus, a wide linear operating range simplifies the data processing [19]. Ideally, an FTIS with high sensitivity, high resolution and a wide linear operation range is desirable.

Surface plasmon resonances [12, 20, 21] are widely used approaches to achieve wide linear operating ranges as well as label-free detection for RI sensors. This type of resonance is commonly realized by integrating two-dimensional (2D) nano- or micro-sized metallic structures onto the fiber facets. However, surface plasmon resonances typically have limited sensitivities in a range of hundreds of nm/RIU and suffer from low Q factors due to the intrinsic ohmic losses of metals [16]. In contrast, dielectric Fabry–Perot interferometer (FPI) can support high-Q resonances, which offer high sensitivity for RI sensors. By deploying the three-dimensional (3D) FPI on the fiber end facets through techniques such as fiber splicing [22], femtosecond laser ablation [23], and two-photon photolithography (TPL) [15, 24], an FTIS with high resolution can be easily realized. However, the working range of an FPI is limited by its narrow FSR. The limitation comes from the intrinsic tradeoff between Q factor and *FSR*. That is, Q factor and *FSR* are inversely proportional to each other via the identity $FSR^{*}Q/\lambda_{res}$ equals to F, where F (finesse parameter) measures the *FWHM* of a FP mode and solely depends on the reflectivity of the cavity mirrors. Specifically, once F is fixed, the *FSR* is inversely proportional to the cavity length, while the Q factor is proportional to the cavity length. To magnify the *FSR* without compromising the Q value, the Vernier effect has been introduced to FPIs by combining two interferometers with a slight difference in their optical path lengths [25]. Albeit the *FSR* of the Vernier envelope exceeds that of the individual FPI, the Vernier methods merely focus on enhancing the sensitivity and the resolution, while leaving the operating range unattended. On the other hand, the combination of the 2D metasurfaces and 3D FP cavities has demonstrated promising results in enhancing the performance of fiber lasers [26]. This scheme has also been reported in studies on on-chip devices [27–29], and has recently sparked further interest in FTISs [13]. Nevertheless, the development of an FTIS with high resolution and a wide linear range remains elusive due to the tradeoff between Q value and *FSR* of the resonance mode.

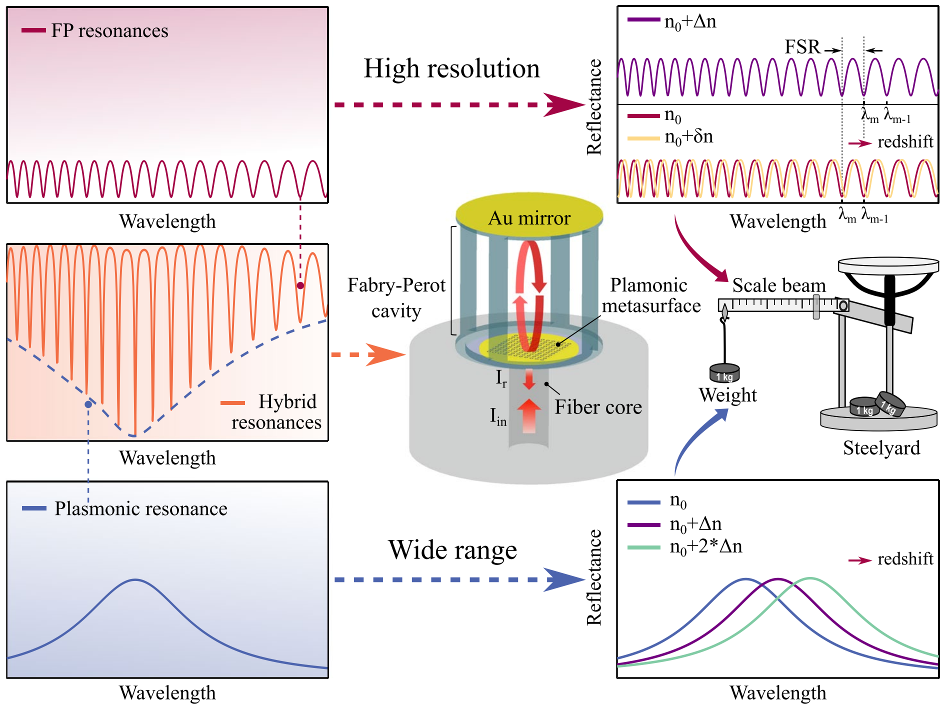

Fig. 1 Configuration and working principle of the metafiber-FPI. The metafiber-FPI is composed of three layers: plasmonic metasurface at the bottom, an open FP cavity in the middle, and a uniform gold film on the top, all integrated onto the end facet of a single mode fiber jumper (SMFJ). The high resolution and wide linear range are realized at the same time by utilizing the hybrid resonance spectrum of the metafiber-FPI, which is characterized by the FP resonances enveloped by a plasmonic resonance. n_0 is the reference RI serving as the origin of the scale beam, Δn hereafter represents the RI period, resulting in a redshift equivalent to an *FSR* of the FP resonances, and δn is the RI change within a Δn. λ_m and λ_{m-1} are two adjacent orders of the FP interference. Once the RI variation is beyond a Δn, the plasmonic resonance could then be used to identify which order ⟩ of Δn that the RI variation belongs to. This scheme effectively extends the operating range and guarantees the resolution by δn induced from the FP resonances

In this study, we propose and demonstrate an FTIS that hybridizes the plasmonic and the FP resonances to achieve simultaneous improvement in the Q factor and the *FSR*. The FTIS features a hybrid-2D-metasurface-and-3D-FP configuration that is integrated on the end facet of optical fibers by our newly developed fabrication methods. The hybrid configuration consists of three layers: a bottom layer of gold plasmonic metasurface on the facet which is referred as the metafiber [30–33], a middle layer of an open polymer-based Fabry–Perot (FP) cavity and a top layer of gold film. The metafiber has been widely adopted to describe the fiber-metasurface hybrid structures, including plasmonic metafibers and dielectric metafibers [30–33]. The whole configuration is hereafter termed as metafiber-Fabry–Perot interferometer (metafiber-FPI). As shown in Fig. 1, a high resolution and a wide linear range of the FTIS are realized simultaneously by indexing the high-Q (but narrow-*FSR*) FP resonances enveloped by a wide-*FSR* (but low-Q) plasmonic resonance. The metafiber-FPI is an optical analog to a steelyard, in which the spectrum of the FP resonances serves as a scale beam, providing precise information about the measurand, while the spectrum of the plasmonic resonance functions like the weight indicating the measuring range. Particularly, once the RI change is beyond a variation period Δn, resulting in a spectral shift beyond an *FSR* of the conventional FPI, the

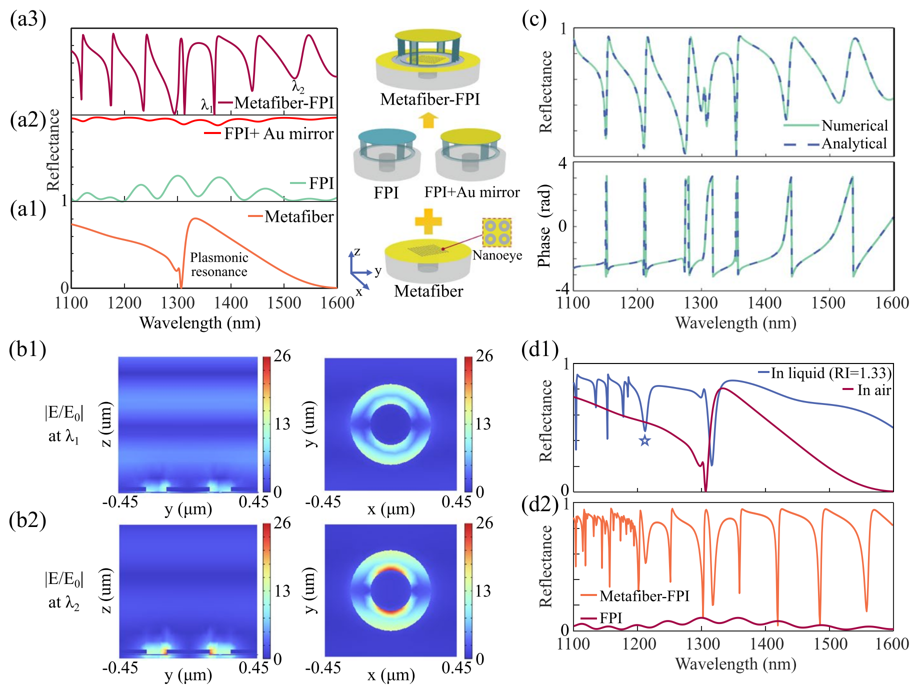

Fig. 2 Optical responses of the metafiber-FPI system. **a** Formation of a metafiber-FPI by combining a metafiber and an FPI with a top gold mirror, and the corresponding reflectance spectra. **b** Electric field distribution ($|E/E_0|$) in the *yz*- and *xy*- planes for two resonance wavelengths at λ_1: 1369 nm in (b1) and λ_2: 1521 nm in (b2). **c** Reflectance and phase spectra of the metafiber-FPI from numerical (green solid line) and semi-analytical (blue dashed line) modeling. (d1) Reflectance spectra of the metafiber in air and in liquid (RI = 1.33). (d2) Reflectance spectra of the metafiber-FPI (orange line) and the FPI (red line) in liquid (RI = 1.33)

FP resonance interrogation becomes invalid. Nevertheless, the linear spectral shift of the plasmonic resonance under the same RI variation can be effectively distinguished owing to its gently evolving but aperiodic envelope. In this way, the FP and plasmonic resonances from the metafiber-FPI collaboratively fulfill both criteria of both high resolution and wide range, which are otherwise mutually exclusive.

Results

Optical resonance of the metafiber-FPI

Figure 2(a) depicts the configuration of the metafiebr-FPI, which combines a metafiber and a polymer-based FPI with a top gold mirror. Plasmonic metasurfaces are situated in the core region of SMFJ to form the metafiber. The nanoeye structure is chosen as the unit cell of the plasmonic metasurfaces due to its extensive study [33]. The nanoeye can provide hybridized plasmonic modes due to the nanodisc and nanohole coupling, which greatly enhance light-matter interactions [20, 33]. The reflectance spectra and electric field distributions of the metafiber, the FPI, FPI with a top gold mirror (FPI + Au mirror), and the metafiber-FPI are simulated using the three-dimensional finite element methods (COMSOL Multiphysics 6.0; see "Numerical modeling" from SI for details). Here, a group of geometric parameters is taken as an example to reveal the physical mechanism behind the resonances of the metafiber-FPI, which is hereafter termed as hybrid resonances. The diameters of the inner nanodisc and outer nanohole are 280 nm and 550 nm, respectively, while the period of the unit cell is 900 nm. The thickness of the bottom nanoeye metasurface and top gold layer are both 55 nm. The open cavity has a total length of 11.5 μm including an air section of 10 μm and a top polymer cover of 1.5 μm. The metafiber exhibits an overall high reflectance, except for the dips around the wavelengths of the plasmonic modes (see in Fig. 2(a1)). In comparison, the FPI, whose end mirrors are respectively fiber substrate and the polymer cover without the gold coating, shows considerably lower reflectance, as depicted by the green curve in Fig. 2(a2). This rather low reflectance arises from the low reflectivity at the fiber-air and polymer-air interfaces [3]. The overall reflectance of the FPI can be greatly improved when its top is coated with a uniform gold film. However, the spectral visibility is deteriorated in the meanwhile, as portrayed by the red curve in Fig. 2(a2). The Q factors of plasmonic modes, and the FP modes with/without the top gold mirror are rather low (<100). However, by merging the metafiber with the FPI + Au mirror to form the metafiber-FPI, the Q factor can be dramatically improved. As demonstrated in Fig. 2(a3), the reflectance spectrum of metafiber-FPI presents a series of hybrid resonances, which are featured by the fingerprint of the FP resonances with an envelope of the plasmonic resonance. Each order of the hybrid resonances has a line shape of Fano resonance due to the interference between the broad plasmonic resonance and the narrow FP resonances [34–36]. The Fano feature is evident from the asymmetric high-Q (maximum ~ 690) spectrum with a large resonance visibility (around 85%) at the resonance wavelength of 1369.5 nm (see "Fano spectrum fitting" from SI for details).

Different orders of the hybrid resonances may have distinct Q factors and visibilities due to their different degrees of hybridization between the plasmonic and the FP modes. To illustrate this effect, Fig. 2(b) compares the electric-field distribution at two resonance wavelengths: λ_1 (1369 nm) and λ_2 (1521 nm). For both resonances, the strongest field enhancement occurs around the nanoeye structure due to the participation of plasmonic modes. Nevertheless, at λ_1, while part of the light energy is confined near the nanoeye's corner (the maximum field enhancement factor is about 14), there is significant portion of light in the FP cavity, whose interference leads to a clear standing wave pattern. In contrast, at λ_2, most of the light is confined around the nanoeye (the maximum field enhancement factor is about 26), leaving a small amount of light resonating within the cavity. The FP resonance is suppressed, and the hybridization degree decreases, which lowers the Q value. However, the penetration of field into liquid and large field enhancement on the other hand may promote the sensitivity of the sensor due to the intense interaction between the field and liquid. Moreover, the wavelength of hybrid resonances can be further tuned by altering the period of the nanoeye metasurface, providing an extra designing degree of freedom to place the high-Q resonance at a desired wavelength. (see "Dependence of reflectance on the period of nanoeye metasurface" from SI for details).

In order to gain a comprehensive understanding of the origin of the high Q spectrum, the reflectance of the metafiber-FPI is analyzed by a semi-analytical model. The semi-analytical model takes into account the multiple reflections of light between the partially transparent plasmonic nanoeye and the top gold mirror [37, 38]. For convenience of revealing the physics, the geometric model is simplified by ignoring the polymer cover. The reflectance for a normal incidence from the fiber substrate is expressed by

$$R = \left| r_{m1} + \frac{e^{-i2\phi} r_{coat} t_m^{\ 2}}{1 - e^{-i2\phi} r_{coat} r_{m2}} \right|^2 \tag{1}$$

where r_{m1}, r_{m2} and are the complex Fresnel reflection coefficients of the metafibers upon which the light impinges from the lower and upper sides of the nanoeye metasurface, respectively, t_m is the transmission coefficient of the metafiber (it is independent on the direction of the incident light due to the reciprocal principle), r_{coat} is the gold mirror's reflection coefficient, $\phi=2\pi nh/\lambda$ is the phase accumulated with n and h being the RI and the length of the cavity, respectively (see "Semi-analytical modeling" from SI for details). The geometric parameters used in the semi-analytical simulations are identical to those of the numerical simulation mentioned above. The r_{m1}, r_{m2}, r_{coat} and t_m are determined separately by numerical modelling. Figure 2(c) depicts the reflectance and phase spectra of the metafiber-FPI. The semi-analytical results are well consistent with the numerical results. Notably, the semi-analytical model simplifies the calculation of the FP cavity, which typically runs for several hours by numerical modeling. Thus, this method offers a time-saving solution to optimize the optical performance of the metafiber-FPI. The Q factors of the hybrid resonances are determined by the reflectivity of the end mirrors, which can also be measured by the finesse parameter F, defined as [6].

$$F = \frac{\pi \sqrt{|r_{m2} r_{coat}|}}{1 - |r_{m2} r_{coat}|} \tag{2}$$

In the conventional FPI, efforts have been made to increase F by introducing highly reflective coatings to both end mirrors [6, 24]. This can efficiently improve the Q factor without compromising the FSR. Similarly, F is increased in the vicinity of the plasmonic resonance peak, where the reflection coefficients of the metafiber (cf. Figure 2(a1)) and the top gold mirror are both high and commensurate with each other. As a result, the $FWHM$ becomes narrower, leading to a higher Q value.

Next, we examine the reflectance spectrum of metafiber immersed in liquid (RI = 1.33). As shown in Fig. 2(d1), the overall reflectance intensity is enhanced compared with the metafiber in air. Besides, more resonance dips of the plasmonic modes are excited at the short wavelength. Notably, a specifical mode at 1212 nm (labelled by the blue open star) is generated due to the RI matching of the substrate and superstrate of the metasurface [39–41]. This RI matching effectively suppresses the radiative loss of the emergent plasmonic mode and endows this mode with a high sensitivity, which will be systematically employed in the steelyard RI sensing (see "Investigation of sensitivity of the newly born plasmonic mode" from SI for details). Additionally, when the metafiber-FPI is immersed in the same liquid, a larger interferometric signal and a deeper resonance visibility is intuitively expected due to the increase in the reflectance of metasurface, (cf. Figure 2(d1). Conversely, the spectral visibility of the FPI alone is predicted to deteriorate, because the RIs of the end mirrors consisting of fiber and polymer are close to that of the liquid, which lowers the reflectivity of the end mirrors [15]. Figure 2(d2) displays the numerical reflectance spectra of the metafiber-FPI and the FPI immersed in the liquid, which verifies the above predictions. Therefore, the incorporation of the metafiber and the top gold mirror to the FPI not only enhances the Q factor,

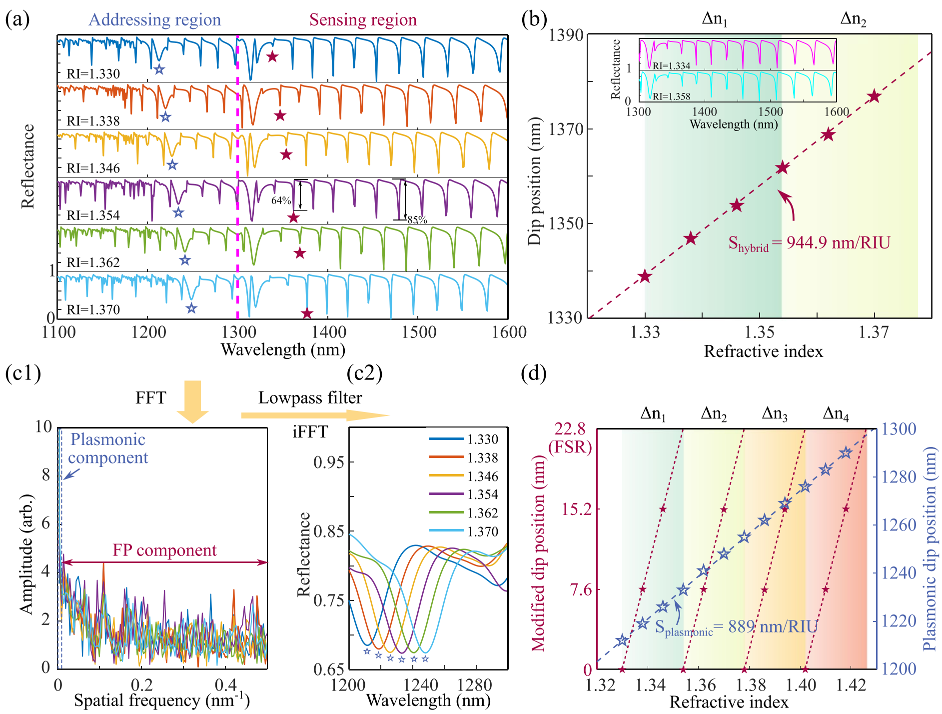

Fig. 3 Working principle of the steelyard RI sensing by using the metafiber-FPI. **a** Reflectance spectra of a metafiber-FPI (period = 900 nm, cavity length = 30 μm) immersed into liquids of different RI values. The spectra are divided into two regions: the addressing and the sensing regions (separated by the magenta dashed line). The plasmonic resonance is labeled by the blue open stars for addressing. One order of the hybrid resonances is labeled by the red solid star for sensing. **b** Dip positions of the hybrid resonance selected in (**a**) versus the RI values. The inset depicts two undistinguishable reflectance spectra despite of different RI values. **c** Data from the addressing region undergoes Fourier analysis to reveal the plasmonic envelope. The abbreviations FFT (fast Fourier transform) and iFFT (inverse fast Fourier transform) are used. (c1) Spatial frequency distribution after FFT. (c2) The plasmonic resonance is extracted after applying a lowpass filter and an iFFT. **d** The steelyard RI sensing diagraph. The positions of the plasmonic resonance and the hybrid resonance versus the RI values are plotted together. The observation window contains four periods of RI

but also provides an essential reflectivity matching for improving spectral visibility in the liquid sensing applications.

Working principle of the steelyard RI sensing

In this section, the working principle of the steelyard RI sensing is theoretically demonstrated. The cavity length is enlarged to 30 μm, while the other geometric parameters remain the same. The numerical simulations of reflectance spectra of the metafiber-FPI with different RI fillings are conducted. The RI values are evenly spaced from 1.33 to 1.43, resulting in 26 groups. For demonstration purposes, 12 groups of data are selected and the first 6 groups are displayed, as shown in Fig. 3(a) (see "Fourier analysis of the overall simulation data" from SI for details). To achieve the steelyard RI sensing, the observation window is divided into two parts: addressing region and sensing region. The data from the sensing region are used to establish a high-resolution sensing scheme, resembling the scale beam of the steelyard that provides the precise information of the measurand. Since the hybrid resonances have similar fingerprints to the original FP resonances while advantageously exhibit higher Q values with larger visibility, the hybrid resonances are hereafter employed for sensing without extracting the FP component from the hybrid resonances. For instance, when the metafiber-FPI is filled with a material having an RI of 1.354, the maximum Q value is approximately 4072 at the wavelength of 1362.4 nm, with the spectral visibility reaching up to 64%. The visibility can exceed 85%, even with a slight decrease in the Q value for a lower-order hybrid resonance at the wavelength of 1454 nm. In order to get the highest resolution, the higher-order hybrid resonance (labeled by red solid star) is selected for sensing. The hybrid resonance dip positions are plotted against the RI values, showing a sensitivity of 944.9 nm/RIU, as illustrated in Fig. 3(b). However, the hybrid resonances within the sensing region shall present almost the same fingerprint when the spectral shift equals to an *FSR*. As shown in the inset of Fig. 3(b), the spectra are almost identical even though the RI values of the liquid are totally different. The undistinguishable fingerprint makes the sensing based on spectral shift invalid and thus grants the metafiber-FPI the maximum RI range or the RI period: Δn equals to *FSR/*sensitivity. Here, the *FSR* is 22.8 nm, and the corresponding Δn is around 0.0241, which is rather close to the RI period (0.0240) of the numerical presetting.

To enlarge the RI sensing range, the data within the addressing region are used to establish a wide-linear-range scheme, which resembles the weight of the steelyard that indicates the measuring range. As discussed in Fig. 2(d1), a higher-order plasmonic mode emerges at 1212 nm when the metafiber is immersed into a liquid (RI = 1.33). The spectrum feature of this plasmonic mode also appears when the metafiber-FPI is filled with liquid, though its line shape shows more asymmetry (as labelled by blue open stars in Fig. 3(a)) due to the hybridization with the FP resonance. Leveraging this plasmonic resonance component, which though has a low Q factor (around 50), enables the determination of the RI period. To systematically extract the plasmonic resonance from the hybrid resonances, the data within the addressing region undergo a successive FFT and low-pass filter operation. The spatial frequencies are depicted in Fig. 3(c1), within which the low frequency component corresponds to the plasmonic resonance [42, 43], and is picked out by applying a low-pass filter operation. Then, by performing an iFFT transformation, the reflectance spectra of the plasmonic resonance are extracted, which almost has the same line shape as that of the bare metafiber in liquid, as shown in Fig. 2(d1) and Fig. 3(c2). The extracted plasmonic resonance dip positions are plotted against the RI values, and the sensitivity ($S_{\text{plasmonic}}$) is obtained thereby by reading the slope of the linearly fitting curve (blue dashed line), as illustrated in Fig. 3(d). To identify which order of RI period (Δn) the measurand falls in, the RI increment of the measurand with coarse resolution is first determined by

$$\delta n_{\text{coarse}} = \frac{\lambda_{\text{plasmonic}} - \lambda^0_{\text{plasmonic}}}{S_{\text{plasmonic}}} \tag{3}$$

where $\lambda_{\text{plasmonic}}$ is the wavelength of the plasmonic dip position extracted from the iFFT results, and $\lambda^0_{\text{plasmonic}}$ is the reference wavelength of plasmonic resonance corresponding to the reference n_0. Subsequently, the order $\rangle$ of RI period (Δn) is determined by

$$\rangle = \left[\frac{\delta n_{\mathrm{coarse}}}{\Delta n}\right] + 1 \tag{4}$$

where $[x]$ is the floor function that provides an integer less or equal to x. By using Eq. (4), a wide linear operating range is built across four consecutive RI periods, as seen in Fig. 3(d).

Next, to better reveal the spectral shift within each *FSR*, the dip position of the hybrid resonances is modified as follow

$$\delta\lambda_{\mathrm{hybrid}} = \lambda_{\mathrm{hybrid}} - \lambda^{0}_{\mathrm{hybrid}} - FSR * \left(\rangle - 1\right) \tag{5}$$

where $\lambda^{0}_{\mathrm{hybrid}}$ is the reference wavelength of hybrid resonance corresponding to n_0, $\lambda_{\mathrm{hybrid}}$ is the actual wavelength of the dip position of the higher-order hybrid resonance directly read from the spectrum. It is clear that $\delta\lambda_{\mathrm{hybrid}}$ starting from 0 and stopping at *FSR*, reflects the net spectral shift within each RI period, which closely resembles a scale beam moving from 0 to the maximum within each weight. By using Eq. (5), the original data and their fitting curve from Fig. 3(b) can be equally divided into several parts and are then reconstructed in Fig. 3(d) with the left vertical axis representing the value of $\delta\lambda_{\mathrm{hybrid}}$. Finally, the RI values of the measurand with fine resolution (n_{fine}) can be expressed by

$$n_{\mathrm{fine}} = n_0 + \frac{\delta\lambda_{\mathrm{hybrid}}}{S_{\mathrm{hybrid}}} + \Delta n * \left(\rangle - 1\right) \tag{6}$$

Notably, Eq. (6) provides a clear picture for determining the RI value of an unknown liquid. Unlike the conventional FPI [15, 24], which presents a limited RI range indicated by the first two items of the right side of Eq. (6), the metafiber-FPI has the capability to measure the RI values even when the spectral shift exceeds an *FSR*. This characteristic of metafiber-FPI enables an RI range enlargement with high linearity, leading to a simpler and more accurate approach for extending the sensing range compared to previous studies [44, 45]. To further demonstrate the steelyard RI sensing capabilities of the metafiber-FPI, the steelyard RI sensing method is applied to the reflectance spectra shown in the inset of Fig. 3(b). Here, $\lambda^{0}_{\mathrm{plasmonic}}$, $\lambda^{0}_{\mathrm{hybrid}}$ and n_0 are 1211.5 nm, 1339 nm and 1.330, respectively, and the other cardinal parameters of each spectrum can be extracted accordingly. Specifically, by using Eqs. (3, 4), the RI increment with coarse resolution and the order $\rangle$ of the unknown liquid could be respectively determined. Then, $\delta\lambda_{\mathrm{hybrid}}$ under the same RI increment could be found by addressing the steelyard RI sensing diagraph. Subsequently, by using Eq. (5), a preliminarily estimated $\lambda_{\mathrm{hybrid}}$ is accordingly calculated. It should be noted that this estimated $\lambda_{\mathrm{hybrid}}$ may deviate from the actual $\lambda_{\mathrm{hybrid}}$ due to the coarse resolution. However, this value provides the key information for user to distinguish which resonance dip shall be addressed and thus read the actual $\lambda_{\mathrm{hybrid}}$ from the reflectance spectrum. Finally, by using Eqs. (5, 6), the resulting RI values for the magenta and cyan spectra are calculated as 1.334 and 1.359, respectively. To quantify the accuracy of the calculations, an error rate is introduced as $|n_{\mathrm{fine}} - n|/n * 100\%$, which is found to be as small as 0.017%.

Fabrication and characterization

To integrate the 2D metasurfaces and 3D FP cavities on the end facets of the optical fiber to form the metafiber-FPI for the steelyard RI sensing, we develop a multi-dimension fabrication method based on our previous works [15, 31, 33]. Figure 4 illustrates the flow chart of the metafiber-FPI processing procedure, which mainly involves the planar fabrication using physical vapor deposition (PVD) for gold film deposition and focused ions beam (FIB) milling, as well as 3D printing using TPL on the fiber end facet. The PVD of gold film and FIB writing processes for fabricating metasurfaces on the tips of the commercial SMFJ are described in detail in our previous works [31, 33]. The thickness of gold films of both the bottom and the top layer is 55 nm, consistent with the simulation setting. As shown in the bottom panel of Fig. 4, FIB (30 kV, 10 pA, Ga^+) is employed to precisely pattern the nanoeye metasurface in the core region of SMFJ to form the metafiber. Next, for TPL, it is important to note that the power density of the TPL laser applied upon the photoresist typically exceeds the damage threshold of gold film [46, 47]. Thus, employing the TPL printing directly on the gold film would inevitably generate excessive heat and cause ablation of gold from the fiber facet. These unexpected defects would degrade the mechanical and optical performances of the FP cavity. (see "Microscopic characterization of the FP cavity directly fabricated on the gold film" from SI for details).

In order to circumvent the undesirable defects during the TPL process, a larger microeye structure with the inner and outer diameters of 60 μm and 100 μm is patterned (30 kV, 600 pA, Ga^+) around the nanoeye metasurface to remove the gold film from the end facet of fiber. TPL is then performed above the metafiber by using a commercial TPL system (PPGT2, Nanoscribe GmbH). Since the entire structure is built on the facet of SMFJ, we have developed and modified the fiber holder based on [15]. The metafiber possesses a plug-and-play property, allowing it to be directly connected to the fiber holder. The polymer-based FP cavity is printed in a layer-by-layer manner, with a cavity pillar height of 30 μm to facilitate the filling of liquid into the cavity. More details about TPL could be found in [7, 15] and SI (see "The photograph of the modified fiber holder and the TPL processing procedures" from SI for details). Finally, the top surface of the polymer cover is coated with another layer of gold film, resulting in the final hybrid configuration of the metafiber-FPI. The SEM image at the stage 3 provides a view of the intact nanoeye metasurface beneath the FP cavity, which demonstrates the good compatibility of multi-dimension fabrication on the end facet of the SMFJ.

During each fabrication stage of the metafiber-FPI, the reflectance spectra are measured using the all-fiber system developed in our previous work [33] (see "Experimental setups for characterization of the reflectance spectra" from SI for details). The reflectance spectra are investigated as functions of the period of nanoeye metasurface. Figure 5(a) depicts the reflectance spectra obtained during the first two fabrication stages. Comparing with the simulation result (cf. Figure 5(c)), the measured spectra of the bare metafibers (solid lines) show broader plasmonic peaks/dips for all periods. This discrepancy arises from the reduced coupling efficiency between the incident light and the metasurface due to the finite size effect [48]. Particularly, only eight periods are encompassed within the mode-field diameter of the single-mode fiber (~ 10 μm at 1550 nm). At the stage 2, the reflectance spectra (dashed lines) also exhibit a clean envelope of the plasmonic resonance, and additionally, periodic ripples stemming from the FP resonances appear. These FP resonances have rather low Q factors due to the poor reflectivity of the top polymer mirror. Figure 5(b) depicts the reflectance spectra obtained at the stage 3, which present high Q values with large spectral visibility due to the introduction of a top gold mirror. Specifically, for a well prepared metafiber-FPI with 900 nm periodicity, the highest Q value (around 2417) is found in the vicinity of the plasmonic peak, where the reflectivity of the metafiber reaches the maximum. Additionally, the largest spectral visibility (around 85%) occurs at the wavelength range of 1189 – 1193 nm. These features are well reproduced in the simulations (see Fig. 5(d)). As depicted in the top panel of Fig. 5(d), the highest Q value (around 2595) is found at the wavelength of 1347.5 nm, almost 23 times larger than that of the conventional FPI (see "Comparison of reflectance spectra between the metafiber-FPI and the FPI" from SI for details). Additionally, the largest spectral visibility is observed around the wavelength of 1268 – 1271 nm, reaching above 88%. The optical properties of our devices surpass those of the works recently published [12, 13, 48], because the new design and simpler fabrication methods enables higher coupling efficiency between the light and plasmonic metasurfaces, as well as the FP cavity.

Moreover, in the vicinity of the plasmonic peaks, the line shape of the spectra at the stage 3 resembles an interesting shape like a folding chair, with the neighborhood asymmetric resonance peak/dip bridged by a flat region (indicated by the semi-transparent rectangles in Fig. 5(b) and Fig. 5(d). This feature region is formed as a result of the modal coupling between the broad plasmonic resonance and the narrow FP resonance. Within this region, the phase change of the plasmonic resonance is slow, while the phase change of the FP resonance is fast (π shift, as shown in the ripples of the dashed lines of Fig. (5a)

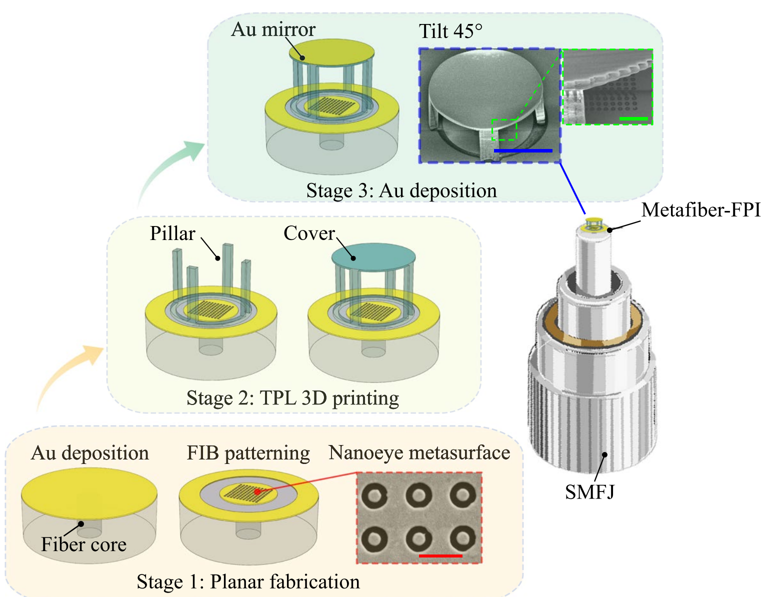

Fig. 4 Schematics of multi-dimension fabrication flow of the metafiber-FPI. The fabrication process consists of three main stages: FIB patterning for the nanoeye metasurface, TPL 3D printing for FP cavity, and PVD for gold mirror. The insets shown at the stage 1 and the stage 3 are scanning electron microscope (SEM) image. The red, blue and green scale bars are 900 nm, 38 μm, and 3.5 μm respectively

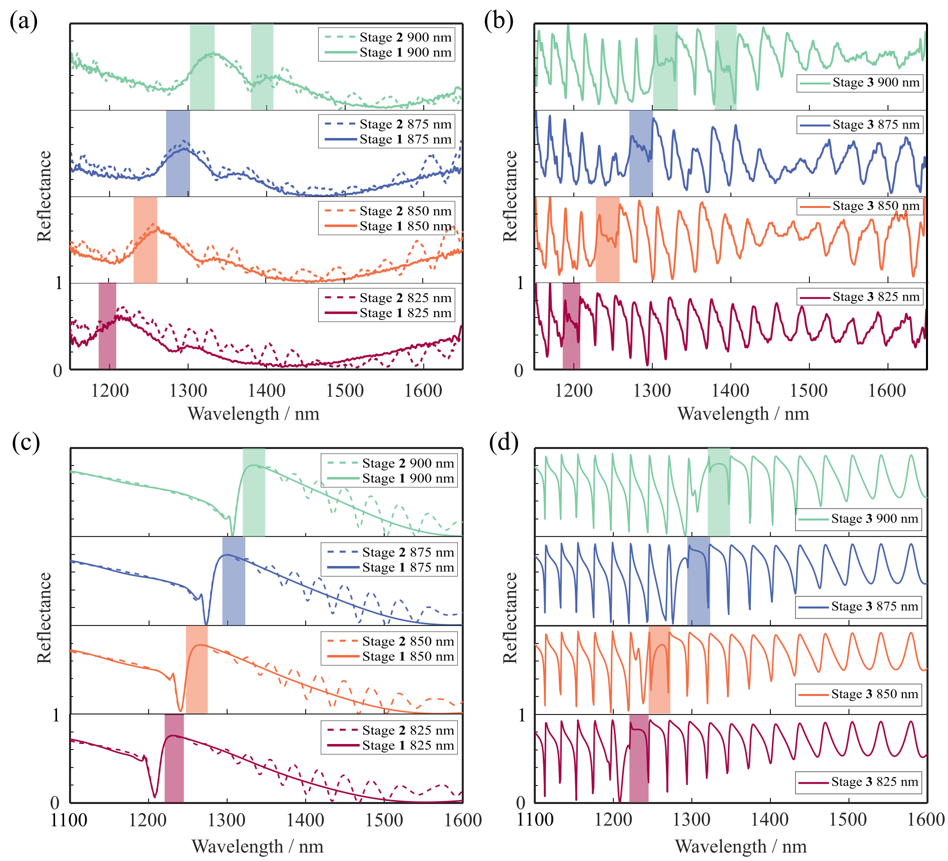

Fig. 5 Evolution of reflectance spectra of the metafiber-FPIs as a function of periods of the nanoeye metasurface. **a**, **b** display the experimental results and (**c**, **d**) stand for the numerical simulations. The semi-transparent rectangles label the region where high Q spectrum and folding-chair-like feature exist in (**b**, **d**)

and Fig. 5(c). As a result, the constructive and destructive interferences between these two resonances subsequently occur at the wavelengths cross the FP resonance, giving rise to the Fano-shaped hybrid resonance peak and dip, as shown in Fig. 5(b) and Fig. 5(d). An extra folding-chair-like feature could be observed in the longer wavelength around 1400 nm, consistent with the appearance of the plasmonic peak in the same spectral range (see Fig. 5(a)). Due to the distinct line shape and the high-Q resonance, the folding-chair-like region can be utilized as a distinguishing feature. For example, the dip position of this hybrid resonance shall be employed in our experiment to determine the RI values.

To verify the steelyard RI sensing, solutions of water-IPA mixtures with varying mole fractions of IPA are utilized. This mixture solution can effectively fill the cavity, and the RI value can be easily tuned, making it an ideal medium for our experiments [15, 24]. The RI values of the solutions are derived from the literature [49] (see "The RI values of solutions versus mole fractions of IPA" from SI for details). We prepare ten groups of solutions with the RI values ranging from 1.3403 to 1.3757, and select six groups for demonstration, as shown in Fig. 6(a). The metafiber-FPI device with 900 nm periodicity is employed due to its highest Q value and distinct feature region. The plasmonic resonance between 1200 and 1300 nm observed in the simulation disappears in the

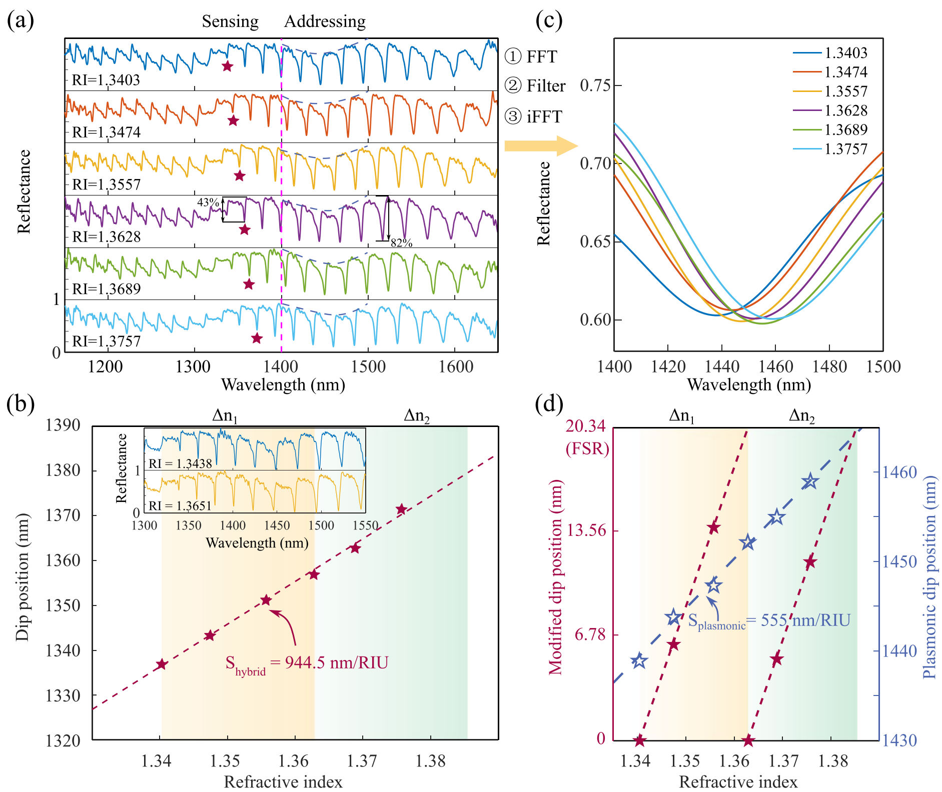

Fig. 6 Experimental verification of the steelyard RI sensing. **a** Reflectance spectra of metafiber-FPI (period = 900 nm, cavity length = 30 μm) immersed into solutions with different RI values. The solution consists of water and isopropanol (IPA) with different mole fractions. The spectra are divided into two regions by the magenta dashed line for sensing and addressing, respectively. One order of the hybrid resonances labeled by red solid star is picked out for sensing. Part of the envelope of the plasmonic resonance is marked by the blue dashed line for addressing. **b** Sensitivity acquisition of the hybrid resonance selected in (**a**). The inset depicts the reflectance spectra with the RI spanning two RI periods. **c** The reflectance spectra of plasmonic resonance after Fourier analysis. **d** Build-up of the steelyard RI sensing diagraph

experiment. This mismatch may evolve from the discrepancy of reflectance spectrum at the stage 1 as well as extra fabrication errors in the subsequent fabrication flow. Nevertheless, the envelope of another plasmonic resonance dip is evident in liquid (marked by the blue dashed line in Fig. 6(a), which can be used for addressing. Specifically, this plasmonic dip envelope stems from the plasmonic dip of the bare metafiber. It appears at the wavelength from 1350 -1400 nm, as seen in the top panel of Fig. 5(a), which offers an appreciable sensitivity among all plasmonic modes (around 390 nm/RIU, see "Investigation of sensitivity of the plasmonic resonance of the metafiber" from SI for details).

As discussed above, the folding-chair-like region features the distinct line shape and a high Q value. Thus, the order of the hybrid resonance within this region (labelled by red solid star) is used to construct a high-resolution sensing scheme, as shown in Figs. 6(a, b). For instance, when the metafiber-FPI is submerged into a solution with the RI value of 1.3628, this hybrid resonance at the wavelength of 1357.5 nm brings the maximum Q value of 3829 with a spectral visibility exceeding 43%. The sensitivity of this hybrid resonance is 944.5 nm/RIU, which is similar to that of our previous work [15]. However, benefitting from the high Q value, the resolution (FoM) is 2664 RIU^{-1}, which is, to our best knowledge, superior to other conventional FPI sensors with similar cavity lengths [50].

Following this step, the plasmonic resonance is precisely extracted from the hybrid resonances by applying the Fourier analysis. The extracted plasmonic resonance presents a similar line shape to that of the bare metafiber, as seen in Fig. 6(c) and Fig. 5(a). The plasmonic resonance dip positions are plotted against the RI values, thereby inducing a sensitivity of 555 nm/RIU, as illustrated in Fig. 6(d). Consequently, the order of RI period (Δn) can be determined by using Eqs. (3, 4) and a linear operating range is built across two successive RI periods. By employing Eqs. (5, 6), the original data and their fitting curve from Fig. 6(b) can be reconstructed in Fig. 6(d), yielding the final steelyard RI sensing diagraph. The accuracy of the steelyard RI sensing is further experimentally demonstrated. Two additional groups of reflectance spectra are chosen, as shown in the inset of Fig. 6(b). Here, $\lambda^0_{\text{plasmonic}}$, $\lambda^0_{\text{hybrid}}$ and n_0 are 1439.1277 nm, 1337.0624 nm and 1.3403, respectively, and the other parameters of each spectrum can be extracted accordingly. The resulting RI values for the blue and yellow spectra are calculated as 1.3433 and 1.3636, respectively, with the minimum error rate of approximately 0.03%.

Moreover, an interesting phenomenon is observed during the experiment. In previous studies, the distilled water is unable to enter the cavity due to the strong capillary force [15, 24]. However, our metafiber-FPI displays improved hydrophilicity, which enables the distilled water to enter and fill the cavity in approximately half an hour (see "Wettability of the metafiber-FPI in the distilled water" from SI for details). This enhanced wettability may be attributed to the introduction of metasurfaces [51, 52], and may offer the potential for label-free biosensors [53], which deserves deep investigations in the future.

Conclusion

Traditional FTISs can barely achieve high resolution and wide linear range simultaneously. In this work, we tackle this problem by incorporating a metafiber and an FPI with a top gold mirror to form the so-called metafiber-FPI, in which the Q factor and FSR are improved together. Leveraging the coupling between the FP resonances and the plasmonic resonance to form the Fano resonances, the highest Q value of ~ 3829 (in liquid) is realized, well consistent with the simulation results. Further, the high Q value is used to ensure a high-resolution (2664 RIU^{-1}) for RI sensing. The physical origin of the Fano resonance is analyzed through a semi-analytical model, which offers a time-saving solution to valid the numerical results as well as to provide insight of the optical properties of coupling system. Further, by employing the Fourier analysis algorisms to reveal the plasmonic background spectrum, the metafiber-FPI is demonstrated to exhibit a wide linear RI sensing range with distinguishable spectral shift of four and two FSRs, in the simulation (1.330 – 1.430) and experiment (1.3403 – 1.3757), respectively. In addition, for fabricating the metafiber-FPIs, the good compatibility of the multi-dimension techniques has been successfully demonstrated on the tips of SMFJs, which provides a robust fabrication method of hybrid configurations on the tiny substrates. The steelyard RI sensing scheme can be further promoted and fuel researches in other types of sensors, and the physical principle behind may shed light on other optical components calling for both high resolution and wide linear working range such as the on-chip spectrometer [54, 55].

Abbreviations

RI	Refractive index
Q	Quality
FSR	Free spectral range
FTIS	Fiber tip integrated sensors
FoM	Figure of merit
FWHM	Full width at half maximum
D	Dimensional
FPI	Fabry–Perot interferometer
TPL	Two-photon photolithography
F	Finesse
metafiber-FPI	Metafiber-Fabry-Perot interferometer
FFT	Fast Fourier transform
iFFT	Inverse fast Fourier transform
PVD	Physical vapor deposition
FIB	Focused ions beam milling
SEM	Scanning electron microscope
SMFJ	Single-mode fiber jumper
IPA	Isopropanol

Supplementary Information

The online version contains supplementary material available at https://doi.org/10.1186/s43074-024-00138-3.

Supplementary Material 1.

Acknowledgements
The authors thank the Westlake Center for Micro/Nano Fabrication for facility support and technical assistance. L.Z. thanks W. Wang at the State Key Laboratory of Extreme Photonics and Instrumentation for assistance with FIB.

Authors' contributions
M.Q. lead the whole research project. L.Z, W.Y and J.Y. conceived the main conceptual ideas. L.Z. designed the configuration of metafiber-FPI. L.Z., X.G. and S.M. prepared samples. L.Z. performed characterizations of metafiber-FPI. L.Z., J.Y., W.Y., Q.N. and M.Q. analyzed the data and wrote the original manuscript.

Funding
The authors gratefully acknowledge the support from the National Natural Science Foundation of China (62275221).

Availability of data and materials
The data that support the findings of this study are available from the corresponding author upon reasonable request.

Declarations

Competing interests
The authors declare no competing interest.

Received: 22 April 2024 Revised: 2 July 2024 Accepted: 25 July 2024
Published: 15 August 2024

References

1. Krohn DA, MacDougall T, Mendez A. Fiber optic sensors: fundamentals and applications. Bellingham: Spie Press; 2014.
2. Gupta BD, Verma R, Srivastava SK. Fiber optic sensors based on plasmonics. World Scientific; 2015.
3. Guggenheim JA, Li J, Allen TJ, et al. Ultrasensitive plano-concave optical microresonators for ultrasound sensing. Nat Photonics. 2017;11:714–9. https://doi.org/10.1038/s41566-017-0027-x.
4. Xiong Y, Xu F. Multifunctional integration on optical fiber tips: challenges and opportunities. Adv Photonics. 2020;2: 064001.
5. Jia Q, Tang W, Yan W, Qiu M. Fibre tapering using plasmonic microheaters and deformation-induced pull. Light Adv Manufact. 2023;4:25–36.
6. Zou M, et al. Fiber-tip polymer clamped-beam probe for high-sensitivity nanoforce measurements. Light Sci App. 2021;10:171.
7. Shang X, et al. Fiber-Integrated force sensor using 3d printed spring-composed Fabry-Perot cavities with a high precision down to tens of piconewton. Adv Mater. 2023;36:2305121.
8. Simin C, Xinggang S, Lei Z, Ning W, Min Q. PDMS-filled micro-spring fabry-perot cavity for temperature sensing. Opt Express. 2023;31:30332–9.
9. Ma X, et al. High-sensitivity and fast-response humidity sensor based on a simple fiber-tip interferometer with thin agarose gel coating. J Lightwave Technol. 2023;41:6824–30.

10. Picelli L, van Veldhoven PJ, Verhagen E, Fiore A. Hybrid electronic–photonic sensors on a fibre tip. Nat Nanotechnol. 2023;18:1162–7.
11. Chen Y, et al. Nanodiamond-based optical-fiber quantum probe for magnetic field and biological sensing. ACS Sensors. 2022;7:3660–70.
12. Consales M, et al. Metasurface-enhanced lab-on-fiber biosensors. Laser Photonics Rev. 2020;14:2000180.
13. Sun X, et al. A quasi-3D Fano resonance cavity on optical fiber end-facet for high signal-to-noise ratio dip-and-read surface plasmon sensing. Light Sci App. 2022;3:665–75.
14. Xiong C, et al. Fiber-tip polymer microcantilever for fast and highly sensitive hydrogen measurement. ACS Appl Mater Interfaces. 2020;12:33163–72.
15. Cao S, et al. Two-photon direct laser writing of micro Fabry-Perot cavity on single-mode fiber for refractive index sensing. Opt Express. 2022;30:25536–43.
16. Xu Y, et al. Optical refractive index sensors with plasmonic and photonic structures: promising and inconvenient truth. Adv Opt Mater. 2019;7: 1801433.
17. Hajshahvaladi L, Kaatuzian H, Moghaddasi M, Danaie M. Hybridization of surface plasmons and photonic crystal resonators for high-sensitivity and high-resolution sensing applications. Sci Rep. 2022;12:21292.
18. Chen R, et al. Nonlinearity synergy: an elegant strategy for realizing high-sensitivity and wide-linear-range pressure sensing. Nat Commun. 2023;14:6641.
19. Lu P, et al. Iontronic pressure sensor with high sensitivity and linear response over a wide pressure range based on soft micropillared electrodes. Sci Bull. 2021;66:1091–100.
20. Liang Y, et al. Subradiant dipolar interactions in plasmonic nanoring resonator array for integrated label-free biosensing. ACS Sensors. 2017;2:1796–804.
21. Chauhan M, Kumar Singh V. Review on recent experimental SPR/LSPR based fiber optic analyte sensors. Opt Fiber Technol. 2021;64:102580.
22. Zhao Y, Wang P, Lv R, Liu X. Highly sensitive airflow sensor based on Fabry-Perot interferometer and Vernier effect. J Lightwave Technol. 2016;34:5351–6.
23. Wei T, Han Y, Li Y, Tsai H-L, Xiao H. Temperature-insensitive miniaturized fiber inline Fabry-Perot interferometer for highly sensitive refractive index measurement. Opt Express. 2008;16:5764–9.
24. Williams JC, Chandrahalim H, Suelzer JS, Usechak NG. Two-photon nanomachining of a micromechanically enhanced optical cavity sensor on an optical fiber tip. Adv Photonics Res. 2022;3:2100359.
25. Gomes AD, Bartelt H, Frazão O. Optical Vernier effect: recent advances and developments. Laser Photonics Rev. 2021;15: 2000588.
26. Flannery J, Al Maruf R, Yoon T, Bajcsy M. Fabry-Pérot cavity formed with dielectric metasurfaces in a hollow-core fiber. ACS Photonics. 2017;5:337–41.
27. Shaltout AM, Kim J, Boltasseva A, Shalaev VM, Kildishev AV. Ultrathin and multicolour optical cavities with embedded metasurfaces. Nat Commun. 2018;9:2673.
28. Fu J, Jin Y, He S. Metasurface for constructing a stable high-*Q* plano-planar open cavity. Adv Opt Mater. 2019;7:1801339.
29. Ossiander M, et al. Metasurface-stabilized optical microcavities. Nat Commun. 2023;14:1114.
30. Ren H, et al. An achromatic metafiber for focusing and imaging across the entire telecommunication range. Nat Commun. 2022;13:4183.
31. Zhang L, et al. 'Plug-and-play' plasmonic metafibers for ultrafast fibre lasers. Light Adv Manufact. 2022;3:653–64.
32. Li C, et al. Metafiber transforming arbitrarily structured light. Nat Commun. 2023;14:7222.
33. Zhang L, et al. Plasmonic metafibers electro-optic modulators. Light Sci App. 2023;12:198.
34. Luk'yanchuk B, et al. The Fano resonance in plasmonic nanostructures and metamaterials. Nat Mater. 2010;9:707–15.
35. Limonov MF, Rybin MV, Poddubny AN, Kivshar YS. Fano resonances in photonics. Nat Photonics. 2017;11:543–54.
36. Gu L, et al. A compact structure for realizing Lorentzian, Fano, and electromagnetically induced transparency resonance lineshapes in a microring resonator. Nanophotonics. 2019;8:841–8.
37. Cencillo-Abad P, Ou J-Y, Plum E, Zheludev NI. Electro-mechanical light modulator based on controlling the interaction of light with a metasurface. Sci Rep. 2017;7:5405.
38. Lan G, Wang Y, Ou J-Y. Optimization of metamaterials and metamaterial-microcavity based on deep neural networks. Nanoscale Advances. 2022;4:5137–43.
39. Auguié B, Barnes WL. Collective resonances in gold nanoparticle arrays. Phys Rev Lett. 2008;101: 143902.
40. Vala M, Ertsgaard CT, Wittenberg NJ, Oh S-H. Plasmonic sensing on symmetric nanohole arrays supporting high-*Q* hybrid modes and reflection geometry. ACS Sensors. 2019;4:3265–74.
41. Kravets VG, et al. Plasmonic surface lattice resonances: a review of properties and applications. Chem Rev. 2018;118:5912–51.
42. Yi D, et al. Interrogation technique analyses of a hybrid fiber optic sensor based on SPR and MMI. Opt Express. 2020;28:20764–72.
43. Gong P, et al. In situ temperature-compensated DNA hybridization detection using a dual-channel optical fiber sensor. Anal Chem. 2021;93:10561–7.
44. Xia F, Zhao Y. RI sensing system with high sensitivity and large measurement range using a microfiber MZI and a photonic crystal fiber MZI. Measurement. 2020;156: 107603.
45. Liu Z, et al. Refractive index SPR sensor with high sensitivity and wide detection range using tapered silica fiber and photopolymer coating. Opt Express. 2023;31:31768–79.
46. Huang H, et al. Effects of substrate on the femtosecond laser-induced damage properties of gold films. Opt Mater. 2018;81:115–21.
47. Gonzalez-Hernandez D, Varapnickas S, Bertoncini A, Liberale C, Malinauskas M. Micro-optics 3D printed via multi-photon laser lithography. Adv Opt Mater. 2022;11:2201701.
48. Scaravilli M, et al. Excitation of bloch surface waves on an optical fiber tip. Adv Opt Mater. 2018;6: 1800477.

49. Herráez JV, Belda R. Refractive indices, densities and excess molar volumes of monoalcohols + water. J Solution Chem. 2006;35:1315–28.
50. Aydin D, Barnes JA, Loock H-P. In-fiber interferometry sensors for refractive index. Appl Phys Rev. 2023;10: 011307.
51. Li Z, et al. Actively switchable beam-steering via hydrophilic/hydrophobic-selective design of water-immersed metasurface. Adv Opt Mater. 2021;9:2100297.
52. Lu J, et al. A Versatile metasurface enabling superwettability for self-cleaning and dynamic color response. Adv Opt Mater. 2021;10:2101781.
53. Li F, et al. Affinity exploration of SARS-CoV-2 RBD variants to mAb-functionalized plasmonic metasurfaces for label-free immunoassay boosting. ACS Nano. 2023;17:3383–93.
54. Sun C, et al. Integrated microring spectrometer with in-hardware compressed sensing to break the resolution-bandwidth limit for general continuous spectrum analysis. Laser Photonics Rev. 2023;17:2300291.
55. Sun C, Yin Y, Chen Z, et al. Tunable narrow-band single-channel add-drop integrated optical filter with ultrawide FSR. PhotoniX. 2022;3:12. https://doi.org/10.1186/s43074-022-00056-2.